Disordered Tm^{3+},Ho^{3+}-codoped CNGG garnet crystal: Towards efficient laser materials for ultrashort pulse generation at ~2 μm

Zhongben Pan,[1,2] Pavel Loiko,[3] Yicheng Wang,[2] Yongguang Zhao,[2,4] Hualei Yuan,[1] Kaiyang Tang,[1] Xiaojun Dai,[1] Huaqiang Cai,[1] Josep Maria Serres,[5] Sami Slimi,[5,6] Ezzedine Ben Salem,[6] Elena Dunina,[7] Alexey Kornienko,[7] Liudmila Fomicheva,[8] Jean-Louis Doualan,[3] Patrice Camy,[3] Weidong Chen,[2,9] Uwe Griebner,[2] Valentin Petrov,[2] Magdalena Aguiló,[5] Francesc Díaz,[5] Rosa Maria Solé,[5] and Xavier Mateos[5,*]

[1]*Institute of Chemical Materials, China Academy of Engineering Physics, Mianyang, 621900, China*

[2]*Max Born Institute for Nonlinear Optics and Short Pulse Spectroscopy, Max-Born-Str. 2a, 12489 Berlin, Germany*

[3]*Centre de Recherche sur les Ions, les Matériaux et la Photonique (CIMAP), UMR 6252 CEA-CNRS-ENSICAEN, Université de Caen Normandie, 6 Boulevard du Maréchal Juin, 14050 Caen Cedex 4, France*

[4]*Jiangsu Key Laboratory of Advanced Laser Materials and Devices, Jiangsu Normal University, Xuzhou, 221116, China*

[5]*Universitat Rovira i Virgili (URV), Física i Cristal·lografia de Materials i Nanomaterials (FiCMA-FiCNA)-EMaS, Marcel.li Domingo 1, 43007 Tarragona, Spain*

[6]*I.P.E.I. of Monastir, Unit of Materials and Organic Synthesis, Monastir 5019, UR17ES31, Tunisia*

[7]*Vitebsk State Technological University, 72 Moskovskaya Ave., 210035 Vitebsk, Belarus*

[8]*Belarusian State University of Informatics and Radioelectronics, 6 Brovki St., 220027 Minsk, Belarus*

[9]*Key Laboratory of Optoelectronic Materials Chemistry and Physics, Fujian Institute of Research on the Structure of Matter, Chinese Academy of Sciences, Fuzhou, 350002 Fujian, China*

ABSTRACT. We report on the growth, structure refinement, optical spectroscopy, continuous wave and femtosecond mode-locked laser operation of a Tm^{3+},Ho^{3+}-codoped disordered calcium niobium gallium garnet (CNGG) crystal. The 2.64 at.% Tm, 0.55 at.% Ho:CNGG is grown by the Czochralski method. Its cubic structure, sp. gr. $Ia\bar{3}d$ - O^{10}_h, a = 12.4952(1) Å, is refined by the Rietveld method revealing a random distribution of Ga^{3+} and Nb^{5+} cations over octahedral and tetrahedral sites. The Ho^{3+} transition probabilities are determined within the Judd-Ofelt theory accounting for an intermediate configuration interaction (ICI). For the $^5I_7 \rightarrow {}^5I_8$ Ho^{3+} transition, the maximum stimulated-emission cross-section σ_{SE} is 0.47×10^{-20} cm^2 at 2080.7 nm. The gain bandwidth of Tm,Ho:CNGG at ~2 μm is >150 nm and the thermal equilibrium decay time - 6.80 ms. The $Tm^{3+} \leftrightarrow Ho^{3+}$ energy transfer parameters are determined. A diode-pumped Tm,Ho:CNGG microchip laser generated 413 mW at 2088.4 nm with a slope efficiency of 15.9%. A continuous wavelength tuning between 1940.3 and 2144.6 nm is demonstrated. Ultrashort pulses as short as 73 fs are achieved at 2061 nm from a Tm,Ho:CNGG laser mode-locked by a GaSb semiconductor saturable absorber mirror at a repetition rate of 89.3 MHz.

Keywords: garnets; crystal structure; optical spectroscopy; holmium ions; energy transfer; laser operation.

1. Introduction

The disordered calcium niobium gallium garnet (shortly CNGG) is a well-known laser host crystal for doping with rare-earth ions (RE^{3+}) [1,2]. It belongs to the cubic crystal class (sp. gr. $Ia\bar{3}d$). The structure disorder originates from a random distribution of the Ga^{3+} and Nb^{5+} cations over the same lattice sites (octahedral and tetrahedral) [3]. The composition of CNGG typically deviates from the stoichiometric one, $Ca_3Nb_{1.5}Ga_{3.5}O_{12}$, so that the structure may accommodate cationic vacancies serving to ensure charge neutrality. A great variety of structural elements in CNGG leads to splitting and inhomogeneous broadening of the spectral bands of the RE^{3+} dopants [3,4], resulting in a glassy-like behavior [1]. CNGG crystals melt congruently at relatively low temperatures around 1430-1470 °C (depending on the composition), so that they can be easily grown by the conventional Czochralski (Cz) method [2]. As a host matrix, CNGG also exhibits attractive thermo-mechanical properties, e.g., moderate thermal conductivity (κ = 4.3 $Wm^{-1}K^{-1}$), weak thermal expansion ($\alpha = 7.8\times10^{-6}$ K^{-1}) and a positive thermo-optic coefficient ($dn/dT = 7.8\times10^{-6}$ K^{-1} at ~1 μm) [3]. CNGG shows a broad transparency range of 0.28 – 8 μm [3] (for oxide crystals) and, thus, it is suitable for short-wave infrared emission at 2 – 3 μm.

The broadband emission properties of RE^{3+} ions in CNGG determine its applications in mode-locked (ML) lasers. The first studies focused on crystals doped with Nd^{3+} and Yb^{3+} ions for laser emission at ~1 μm and, recently, interesting results were achieved in the mode-locked operation regime [5-8]. Ma *et al.* demonstrated sub-50 fs soliton pulses (47 fs, with external compression) at 1061 nm from a Yb^{3+},Na^{+}:CNGG laser ML by a SEmiconductor Saturable Absorber Mirror (SESAM) [8].

Furthermore, the interest shifted to the spectral range of ~2 μm. Such emission is eye-safe and it spectrally overlaps with absorption lines of atmospheric and bio-species such as H_2O or CO_2. Ultrafast lasers at ~2 μm are of practical importance for highly localized surgery (medicine), soft material processing, frequency comb generation, molecular spectroscopy and supercontinuum generation. They are used as seed sources for frequency down-conversion into mid-infrared and terahertz (THz) spectral ranges [9]. It is common to achieve laser emission at ~2 μm with Tm^{3+} and Ho^{3+} dopant ions.

Tm^{3+}-doped CNGG crystals were first studied by Voronko *et al.* [10,11] and interesting advances have been published recently. Pan *et al*. reported on the Cz crystal growth, spectroscopy and continuous-wave (CW) laser operation of CNGG codoped with active Tm^{3+} and passive Na^{+}(Li^{+}) cations serving for charge compensation [12]: a diode-pumped Tm^{3+},Na^{+}:CNGG laser generated 1.05 W at 2007.7 nm with a slope efficiency of 35%.

Broadband wavelength tuning in a Tm^{3+},Li^{+}:CNGG laser (tuning range: 224 nm) was realized [12]. Wang *et al.* reported on a Tm^{3+},Li^{+}:CNGG laser ML by a single-walled carbon nanotube (SWCNT) saturable absorber (SA) delivering pulses as short as 78 fs without external compression at 2017 nm, at a pulse repetition rate of 86 MHz [13]. Slightly longer pulses (84 fs) were generated in a similar laser based on a Tm^{3+},Na^{+}:CNGG crystal [14].

The Holmium ion (Ho^{3+}, electronic configuration: $[Xe]4f^{10}$) is attractive for laser emission at wavelengths slightly above 2 μm owing to the $^5I_7 \rightarrow {}^5I_8$ electronic transition. This emission is red-shifted with respect to that of the Tm^{3+} ion and is thus more attractive for ML lasers because it avoids the unwanted overlap with the structured water vapor absorption in the atmosphere [15]. Two routes to excitation of Ho^{3+} ions are known. The first one is the so-called in-band pumping, exciting directly to the Ho^{3+} upper laser level ($^5I_7$) which benefits from a high laser efficiency [16] being suitable for power scaling [17]. However, the required pump sources (e.g., powerful Tm fiber lasers or GaSb laser diodes) are expensive and still under development. The second pump scheme is relying on Tm^{3+},Ho^{3+} codoping [18]. Tm^{3+} ions can be pumped by commercial AlGaAs laser diodes emitting at ~0.8 μm transferring part of the energy of the electronic excitation to the Ho^{3+} ions. Despite the limited power scaling of Tm,Ho lasers owing to thermal effects, the codoping scheme may greatly increase the gain bandwidth of the material by combining the individual emissions from both Tm^{3+} and Ho^{3+} ions. This is an attractive feature for ML laser development [19].

To date, very limited information exists about Ho^{3+}-doped CNGG crystals. Ryabochkina *et al.* reported on the Cz growth, spectroscopy and in-band pumped laser performance of Ho:CNGG delivering 2.1 W at 2095 nm with a slope efficiency of 37% [20]. Xue *et al.* have grown such crystals by the μ-pulling down method [21]. Very recently, we demonstrated a Tm,Ho:CNGG laser ML by a SWCNT-SA delivering 83-fs pulses (without external compression) at 2081 nm at a repetition rate of 102 MHz [22].

In the present paper, we study in detail the structure, spectroscopic and laser properties of the disordered Tm,Ho:CNGG garnet with the goal of developing an efficient laser material for sub-100 fs ML lasers at ~2 μm.

2. Experimental section

2.1. Crystal growth

A 3.0 at.% Tm^{3+}, 0.5 at.% Ho^{3+} (in the melt) doped CNGG single crystal was grown by the Cz method using Ar atmosphere in an Ir crucible. The starting materials, $CaCO_3$ (purity: 4N), Nb_2O_5 (4N), Ga_2O_3 (5N), Tm_2O_3 (5N) and Ho_2O_3 (5N), were first weighed according to

the chemical formula $(Tm_3Ga_5O_{12})_{0.03}(Ho_3Ga_5O_{12})_{0.005}Ca_3Nb_{1.6875}Ga_{3.1875}O_{12})_{0.965}$. To compensate the volatilization of Ga_2O_3 during the synthesis of the polycrystalline material and the crystal growth, an excess of 1.0 wt% Ga_2O_3 was added. The equation of the chemical reaction reads:

$$5.79CaCO_3 + 1.6284375Nb_2O_5 + 3.2509375Ga_2O_3 + 0.09Tm_2O_3 + 0.015Ho_2O_3 \rightarrow$$
$$2(Tm_3Ga_5O_{12})_{0.03}(Ho_3Ga_5O_{12})_{0.005}(Ca_3Nb_{1.6875}Ga_{3.1875}O_{12})_{0.965} + 5.79CO_2\uparrow. \quad (1)$$

The components of the growth charge were first mixed, ground and heated at 1173 K in a Pt crucible for 10 h to decompose $CaCO_3$. After the crucible was cooled down to room temperature (RT, 293 K), the mixture was pressed into pellets and reheated at 1373 K for 15 h to synthesize the Tm,Ho:CNGG polycrystalline material through solid-state reaction. The latter was placed into an Ir crucible and melted by an intermediate-frequency heater. As a seed for crystal growth, an oriented along the [111] direction Yb;CNGG was used. During the crystal growth process, the pulling rate varied from 0.5 to 1.0 mm/h and the crystal rotation speed was kept at 8 to 15 revolutions per minute (rpm). After the growth was completed, the crystal was cooled down to RT at a stepped rate of 15 to 25 °K/h.

For spectroscopic studies, we also grew a singly Ho^{3+}-doped CNGG crystal using a similar methodology.

2.2. Characterization

The actual concentration of the dopant ions (Tm^{3+} and Ho^{3+}) was determined by inductively-coupled plasma mass spectrometry (ICP-MS, Agilent). The X-ray powder diffraction pattern was measured at room temperature using a Bruker D2 Phaser diffractometer for diffraction angles 2θ in the range of 10 - 80° with Cu $K_{\alpha 1}$ radiation (1.54051 Å).

The thermogravimetric (TG) analysis and differential scanning calorimetry (DSC) were carried out on a simultaneous Mettler-Toledo TGA/DSC 2/1600 thermal analyzer in a flowing N_2 atmosphere. The sample was enclosed in a corundum crucible and heated from room temperature to 1600°C at a heating rate of 1.5°C/min.

The Raman spectrum was measured using a confocal Raman microscope (Renishaw inVia) equipped with an ×50 objective and an Ar^+ ion laser (λ = 514 nm).

For the spectroscopic and laser studies, we cut rectangular elements with a thickness (t) of 3...6 mm and aperture of 3×3 mm^2 using the annealed crystal boule. They were oriented for light propagation along the [111] crystallographic direction.

All the spectroscopic studies were performed at room temperature (RT, 293 K). The absorption spectra in the range of 300-2200 nm were measured using a CARY 5000 (Varian)

spectrophotometer; the spectral bandwidth (SBW) was 0.2 nm. The luminescence spectrum was measured using an optical spectrum analyzer (OSA, AQ6375B, Yokogawa, SBW = 0.1 nm) whose spectral response was calibrated using a Hg lamp. The excitation was from a Ti:Sapphire laser tuned to 802 nm. For the luminescence decay studies, we used a nanosecond optical parametric oscillator (OPO, Horizon, Continuum) as the excitation source and the detection system comprising a ¼-m monochromator (Oriel 77200), an InGaAs detector and an 8-GHz digital oscilloscope (DSA70804B, Tektronix). The measurements were performed on a crashed sample employing a pinhole to eliminate the radiation trapping effect.

3. Crystal growth and structure

3.1. Crystal growth

The as-grown Tm,Ho:CNGG crystal boule is shown in Figure 1(a). It had a cylindric shape with a uniform cross-section in the central part of the boule (dimensions: diameter (ϕ): 25 mm × length: 35 mm). The cross-section was circular, which is typical for the Cz growth method. The crystal was transparent and neither cracks nor inclusions were observed. An inspection of the boule with a He-Ne laser revealed no scattering centers. The as-grown crystal was yellow-colored, which is attributed to the absorption of color centers in the visible due to the cationic vacancies, a typical behavior for CNGG-type crystals [3]. To eliminate the color centers, the crystal was annealed in air. First, it was heated from RT to 1373 K for 60 h, then it was kept at this temperature for 90 h and finally cooled down to RT for 60 h. As a result, the transparency of the crystal greatly improved, and its color changed to light-yellow, see Figure 1(b).

The actual concentration of the dopant ions was $N_{Tm} = 3.24\times10^{20}$ cm^{-3} (2.64 at.%) and $N_{Ho} = 6.76\times10^{19}$ cm^{-3} (0.55 at.%). Thus, the segregation coefficients for the rare-earth ions, $K_{RE} = N_{crystal}/N_{melt}$ were $K_{Tm} = 0.88$ and $K_{Ho} = 1.10$. For the singly Ho^{3+}-doped CNGG crystal grown for comparison, the actual doping level was measured to be 0.55 at.% Ho.

The results of the TG-DSC analysis are shown in Figure 2. The thermogravimetric (TG) analysis shows that Tm,Ho:CNGG has nearly no weight loss in the whole studied temperature range. From the heating curve of the DSC, only one endothermic peak was observed which corresponds to the melting point. The melting temperature of Tm,Ho:CNGG, taken as the onset temperature of this peak, is 1698 K (here, we define the onset temperature as the intersection of the tangent in the flat zone before the peak and the tangent in the maximum slope of the

peak). Tm,Ho:CNGG is completely melted at the peak temperature of 1707 K and the cubic phase is stable below the melting temperature.

3.2. Structure refinement

The structure and the phase purity of the as-grown crystal were confirmed by X-ray powder diffraction (XRD), Figure 3(a).

The crystal structure was refined using the Rietveld method, see the details in Table 1. As starting atomic coordinates, we used the data from the undoped CNGG crystal [23]. The starting occupancy factors were taken from [24], considering the determined actual doping concentrations for Tm^{3+} and Ho^{3+}. Tm,Ho:CNGG is cubic (sp. gr. $Ia\bar{3}d$ - O^{10}_h, No. 230) and isostructural to the undoped CNGG crystal. The lattice constant a = 12.4952(1) Å and the unit-cell volume V = 1950.87 $Å^3$ (the number of formula units in the unit-cell Z = 8). The calculated crystal density is ρ_{calc} = 5.064 g/cm^3. The R-factors for the refinement were as follows: R_{wp} = 7.76% and R_{exp} = 6.13% (the reduced χ-squared value $\chi^2 = (R_{wp}/R_{exp})^2$ = 1.60). The determined fractional atomic coordinates (x, y, z) are listed in Table 2. No other phases except of the cubic one are found in the pattern.

According to the determined atomic coordinates, we drew the structure of Tm,Ho:CNGG. Figure 3(b) shows its projection in the ***b*-*c*** plane. CNGG-type crystals belong to the family of cubic multicomponent garnets with a general formula $\{A\}_3[B]_2(C)_3O_{12}$, where {A}, [B], and (C) are dodecahedral (Wyckoff symbol: 24*c*), octahedral (16*a*), and tetrahedral (24*d*) sites, respectively [3]. Stoichiometric CNGG has a chemical formula of $Ca_3Nb_{1.5}Ga_{3.5}O_{12}$, or, equivalently, $\{Ca_3\}[Nb_{1.5}Ga_{0.5}](Ga_3)O_{12}$. Such a garnet can be synthesized only by precipitation at a temperature <1633 K in the form of polycrystalline material [1]. For a real crystal, its composition deviates from the stoichiometric one, e.g., let us consider the studied crystal of Tm,Ho:CNGG. The Ca^{2+} ions are located in dodecahedral sites (with a coordination number, C.N. = VIII). The rare-earth ions (Tm^{3+} and Ho^{3+}, in our case) replace for the Ca^{2+} ones in these sites. The corresponding ionic radii for VIII-fold oxygen coordination are R_{Ca} = 1.12 Å, R_{Tm} = 0.994 Å and R_{Ho} = 1.105 Å [25] which explains the observed decrease of the lattice constant for the Tm,Ho:CNGG crystal as compared to undoped CNGG (a = 12.5969(1) Å [26]). There are four shorter (2.366 Å) and four longer (2.499 Å) metal - oxygen (M - O) interatomic distances in the $[Ca|Tm|HoO_8]$ dodecahedra, Figure 4. The Ga^{3+} and Nb^{5+} cations are randomly distributed over both the octahedral (C.N. = VI) and tetrahedral (C.N. = IV) sites, see the occupancy factors (O.F.) in Table 2. The corresponding

M – O bond lengths are 2.024 Å (×6) and 1.642 Å (×4), Figure 4. The bond lengths and geometric parameters of the [MO_n] polyhedrons in Tm,Ho:CNGG are summarized in Table 3.

The random distribution of the Ga^{3+} and Nb^{5+} cations over the octahedral and tetrahedral sites determines the disordered crystal structure. The inhomogeneous broadening of the spectral bands of the rare-earth ions in Ca^{2+} sites occurs due to the various multi-ligands in the second coordination sphere. The shortest intermetallic distances are: Ca|Tm|Ho – Ca|Tm|Ho = 3.692 Å (×6), Ca|Tm|Ho – Nb1|Ga1 = 3.370 Å (×4) and Ca|Tm|Ho – Nb2|Ga2 = 3.692 Å (×4) and 3.014 Å (×2).

According to the structure refinement data, the actual crystal composition is the following: $\{Ca_{2.9043}Tm_{0.0792}Ho_{0.0165}\}[Nb_{1.42}Ga_{0.58}](Ga_{2.754}Nb_{0.246})O_{12}$.

3.3. Raman spectroscopy

Raman spectroscopy is known to be a sensitive tool to study the structural features of CNGG crystals [1,3]. The unpolarized Raman spectrum of Tm,Ho:CNGG is shown in Figure 5.

The two groups of vibrations which are most sensitive to structure alteration are found in the long-frequency part of the Raman spectra of CNGG-type crystals (at ~700-900 cm^{-1}) [1]. They are assigned to the symmetric stretching modes (ν_s) of isolated metal oxygen tetrahedra [$M2O_4$]. For Tm,Ho:CNGG, the tetrahedral sites are occupied by both Ga^{3+} and Nb^{5+} cations. The lines at lower frequencies correspond to the [$Ga2O_4$] groups and those at higher frequencies – to the [$Nb2O_4$] ones. The appearance of satellite peaks indicates the structural distortion of the [$M2O_4$] tetrahedra due to a nearby cationic vacant position [1]. At lower frequencies, there are two lines at 746 cm^{-1} (C_1, vacancies) and at 777 cm^{-1} (C_2, undistorted [$Ga2O_4$]). At higher frequencies, there are such at 827 cm^{-1} (C_4, undistorted [$Nb2O_4$]) and 869 cm^{-1} (C_5, vacancies). The relative intensity of the satellite C_1 and C_5 lines is weak indicating a moderate distortion of the [$M2O_4$] tetrahedra. Note that the introduction of RE^{3+} ions (Tm^{3+} and Ho^{3+} in our case) in dodecahedral sites reduced the concentration of vacancies in these sites and in the octahedral ones while it almost did not affect those in the tetrahedral sites [3]. The RE^{3+} ion effect is revealed by a frequency shift of the C_2 and C_4 lines. Indeed, for stoichiometric undoped CNGG, they are found at 763 cm^{-1} and 832 cm^{-1}, respectively [1]. The broad pedestal seen in the long-frequency part is due to the luminescence of the Ho^{3+} ion.

4. Optical spectroscopy

4.1. Judd-Ofelt modeling: Ho^{3+} ions

The transition probabilities for the Tm^{3+} ion in CNGG were analyzed previously using the standard Judd-Ofelt (J-O) theory [12]. Consequently, we focused on the J-O analysis only for the Ho^{3+} ion. To this aim, the absorption spectra were measured for both Tm,Ho:CNGG (codoped) and Ho:CNGG (singly doped) crystals, Figure 6. Here, the assignment of the Tm^{3+} and Ho^{3+} transitions is after [27]. The analysis of the Ho^{3+} transitions in absorption for both crystals yielded similar results. Below, for clarity, we will describe only the results achieved for Ho:CNGG.

The calculations were performed using the standard J-O theory [28,29] and its modification accounting for an intermediate configuration interaction (ICI) [30,31]. The reduced squared matrix elements $U^{(k)}$, $k = 2, 4, 6$ for Ho^{3+} transitions in absorption and emission were taken from [32]. The refractive indices were calculated from the Sellmeier equation [3]. The J-O formalism was applied to electric-dipole (ED) contributions to intensities of the 4f-4f Ho^{3+} transitions. The contribution of magnetic-dipole (MD) transitions with $\Delta J = J - J' = 0, \pm 1$ was calculated separately within the Russell–Saunders approximation on wave functions of Ho^{3+} under the assumption of a free-ion.

For the standard J-O theory, the ED line strengths of the J → J' transitions $S^{ED}(JJ')$ are calculated as [28,29]:

$$S_{calc}^{ED}(JJ') = \sum_{k=2,4,6} U^{(k)}\Omega_k, \tag{1a}$$

$$U^{(k)} = \langle (4f^n)SLJ \,||\, U^k \,||\, (4f^n)S'L'J' \rangle^2. \tag{1b}$$

Here, $U^{(k)}$ are the reduced squared matrix elements and Ω_k are the intensity (J–O) parameters (for both, $k = 2, 4, 6$).

Within the ICI approximation, the ED line strengths are given by [31]:

$$S_{calc}^{ED}(JJ') = \sum_{k=2,4,6} U^{(k)}\tilde{\Omega}_k, \tag{2a}$$

$$\tilde{\Omega}_k = \Omega_k[1 + 2R_k(E_J + E_{J'} - 2E_f^0)]. \tag{2b}$$

The J-O (intensity) parameters $\tilde{\Omega}_k$ are the linear functions of energies of the two multiplets (E_J and $E_{J'}$) involved in the transition, where E_f^0 is the mean energy of the $4f^n$ configuration and R_k ($k = 2, 4, 6$) are the parameters representing the configuration interaction. There are 6 free parameters, namely Ω_k and R_k ($k = 2, 4, 6$).

The measured and calculated absorption oscillator strengths (f^{Σ}_{exp} and f^{Σ}_{calc}, respectively) are listed in Table 4. The root-mean-square (rms) deviation between these values is lower when using the ICI approximation (1.260) as compared to the standard J-O theory (2.784). Moreover,

the former model predicts better the oscillator strength for the $^5I_8 \rightarrow {}^5I_7$ transition. Thus, we used the ICI model for further calculations. The determined intensity parameters (Ω_k and R_k for the ICI approximation and Ω_k for the standard J-O theory) are listed in Table 5.

The probabilities of spontaneous radiative transitions $A^{\Sigma}_{calc}(JJ')$, the luminescence branching ratios $B(JJ')$ and the radiative lifetimes of the excited-states τ_{rad} (up to $^5S_2+{}^5F_4$) are listed in Table 6 (as calculated within the ICI approximation).

The radiative lifetime of the upper laser level of Ho^{3+} ($^5I_7$) in Tm,Ho:CNGG is 8.41 ms. Xue *et al.* determined the $^5I_7$ luminescence lifetime for 0.5 at.% Ho:CNGG as 7.07 ms [21] which agrees well with our calculation. Ryabochkina *et al.* evaluated τ_{rad} ~13 ms from the reciprocity method which seems to be notably overestimated [20].

4.2. $Tm^{3+} \leftrightarrow Ho^{3+}$ energy transfer

Tm^{3+},Ho^{3+} codoped materials can be easily excited at ~0.8 μm (to the $^3H_4$ Tm^{3+} state). Due to the efficient cross-relaxation for neighbor Tm^{3+} ions, $^3H_4 + {}^3H_6 \rightarrow {}^3F_4 + {}^3F_4$, the lower-lying Tm^{3+} excited-state is populated. As the barycenter of the $^3F_4$ Tm^{3+} state is located slightly above that of the $^5I_7$ Ho^{3+} state, an efficient $Tm^{3+} \rightarrow Ho^{3+}$ energy-transfer (ET) may take place leading to the $^5I_7 \rightarrow {}^5I_8$ Ho^{3+} emission at >2 μm. Figure 7(a) shows the luminescence spectrum of the Tm,Ho:CNGG crystal.

The Tm,Ho:CNGG emission is broadband and it spans from ~1.6 to 2.12 μm originating from both the $^3F_4 \rightarrow {}^3H_6$ Tm^{3+} and $^5I_7 \rightarrow {}^5I_8$ Ho^{3+} transitions. As compared to a singly Tm^{3+}-doped crystal, the spectrum extends to longer wavelengths.

To determine the parameters of the bidirectional $^3F_4$ (Tm^{3+}) $\leftrightarrow$ $^5I_7$ (Ho^{3+}) ET and to assess the suitability of Tm,Ho:CNGG for laser operation, we performed luminescence decay studies. The luminescence was excited at 1615 nm (directly to the $^3F_4$ Tm^{3+} state) and monitored at 1800 nm (purely Tm^{3+} emission) and at 2080 nm (purely Ho^{3+} emission).

The measured luminescence decay curves plotted in a semi-log scale are shown in Figure 7(b). For the Tm^{3+} ion, the luminescence intensity first decreases fast (within few hundreds of μs) and then the decay becomes single-exponential. For Ho^{3+}, a fast rise of luminescence intensity is observed which is synchronized with the Tm^{3+} decay, indicating the ET. The decay of Ho^{3+}, 1 ms after the excitation pulse is also single-exponential with the same time constant as for Tm^{3+}, indicating a thermal equilibrium in the Tm^{3+},Ho^{3+} system.

The measured luminescence decay curves were fitted by the model of Walsh *et al.* [33]:

$$\frac{n_2(t)}{n_2(0)} = \frac{\beta}{\alpha+\beta}\exp(-t/\tau) + \frac{\alpha}{\alpha+\beta}\exp(-(\alpha+\beta)t), \qquad (3a)$$

$$\frac{n_7(t)}{n_7(0)} = \frac{\alpha}{\alpha+\beta}\exp(-t/\tau) - \frac{\alpha}{\alpha+\beta}\exp(-(\alpha+\beta)t)\cdot \quad (3b)$$

Here, t is the time after the excitation pulse, n_2 and n_7 are the fractional populations of the $^3F_4$ Tm^{3+} and $^5I_7$ Ho^{3+} manifolds, $\alpha = P_{28}N_{Ho}$ and $\beta = P_{71}N_{Tm}$ are the transfer rates, P_{28} is the parameter of the direct nonradiative transfer of energy $Tm^{3+} \rightarrow Ho^{3+}$, P_{71} is the parameter of the back ET, $Ho^{3+} \rightarrow Tm^{3+}$ and τ is the thermal equilibrium decay time. The result of the fitting is shown in Figure 7(b). The best-fit parameters are $P_{28} = 5.917\times10^{-23}$ $cm^3\mu s^{-1}$, $P_{71} = 0.679\times10^{-23}$ $cm^3\mu s^{-1}$ and $\tau = 6.80$ ms. The determined τ value is in between the radiative lifetimes for the $^3F_4$ Tm^{3+} state (4.11 ms [12]) and the $^5I_7$ Ho^{3+} state (8.41 ms, this work).

The ratio of the ET parameters, $\Theta = P_{71}/P_{28}$, referred to as the equilibrium constant, is 0.115. It shows how the Tm^{3+} and Ho^{3+} ions share the excitation energy and its value highlights the predominantly direct $Tm^{3+} \rightarrow Ho^{3+}$ ET. The value of Θ for Tm,Ho:CNGG is close to that for Tm,Ho:YAG ($\Theta = 0.12$) [33]. The fractional population of Ho^{3+} ions in the $^5I_7$ manifold in the steady-state regime $f_{Ho} = \alpha/(\alpha+\beta) > 64\%$ and thus the fractional population of Tm^{3+} ions in the $^3F_4$ manifold is $f_{Tm} = 1 - f_{Ho} < 36\%$. These values further emphasize the feasibility of Tm,Ho:CNGG crystals for efficient Ho laser operation.

4.3. Transition cross-sections

The absorption cross-sections, σ_{abs}, for the $^3H_6 \rightarrow {}^3H_4$ Tm^{3+} transition in Tm,Ho:CNGG are shown in Figure 8(a). The maximum $\sigma_{abs} = 0.54\times10^{-20}$ cm^2 at 786.3 nm and the full width at half maximum (FWHM) of the absorption band is 28.4 nm. Thus, Tm,Ho:CNGG is very attractive for pumping with AlGaAs laser diodes emitting at ~0.8 μm due to the low sensitivity of the pump absorption to the temperature drift of the diode wavelength.

The absorption, σ_{abs}, and stimulated-emission (SE), σ_{SE}, cross-sections for the $^3F_4 \leftrightarrow {}^3H_6$ Tm^{3+} and $^5I_7 \leftrightarrow {}^5I_8$ Ho^{3+} transitions at ~2 μm are summarized in Figure 8(b). The SE cross-sections were calculated using the Füchtbauer–Ladenburg (F-L) formula [34]:

$$\sigma_{SE}(\lambda) = \frac{\lambda^5}{8\pi\langle n\rangle^2 \tau_{rad} c} \frac{W'(\lambda)}{\int \lambda W'(\lambda)\mathrm{d}\lambda}, \quad (4)$$

where λ is the wavelength, $<n>$ is the refractive index at the mean emission wavelength $<\lambda_{em}>$ calculated using the Sellmeier formulas [3], c is the speed of light, τ_{rad} is the radiative lifetime of the emitting level ($^3F_4$ for Tm^{3+} and $^5I_7$ for Ho^{3+}) and $W'(\lambda)$ is the luminescence spectrum calibrated for the spectral response of the set-up. For the Tm^{3+} ion, $\tau_{rad}(^3F_4) = 4.11$ ms and for Ho^{3+}, $\tau_{rad}(^5I_7) = 8.41$ ms. The results for Tm^{3+} were previously described [12], so that we focus primarily on the Ho^{3+} ion.

For the $^5I_8 \rightarrow {}^5I_7$ Ho^{3+} transition in absorption, the maximum is $\sigma_{abs} = 0.46\times10^{-20}$ cm^2 at 1920.2 nm. The SE cross-section for this transition in emission is $\sigma_{SE} = 0.47\times10^{-20}$ cm^2 at 2080.7 nm and the emission bandwidth (FWHM) $\Delta\lambda_{em}$ is 70.2 nm.

The transitions of both Tm^{3+} and Ho^{3+} ions at ~2 μm represent a quasi-three level laser scheme with reabsorption. Thus, to estimate the laser wavelength, the tuning range and the gain bandwidth, the gain spectra are calculated:

$$\sigma_{g,Tm(Ho)} = \beta_{Tm(Ho)}\sigma_{SE,Tm(Ho)} - (1-\beta_{Tm(Ho)})\sigma_{abs,Tm(Ho)}, \quad (5)$$

where, $\beta_{Tm} = N_2(^3F_4)/N_{Tm}$ and $\beta_{Ho} = N_7(^5I_7)/N_{Ho}$ are the inversion levels for Tm^{3+} and Ho^{3+} ions, respectively, and N_2 and N_7 are the populations of the $^3F_4$ Tm^{3+} and $^5I_7$ Ho^{3+} upper laser levels, respectively. In the case of a codoped material, the $\sigma_{g,Tm}$ and $\sigma_{g,Ho}$ spectra cannot be treated independently and cannot be used directly to explain the spectral behavior of wavelength tunable or ML lasers because the populations of the excited-states of Tm^{3+} and Ho^{3+} ions are linked to each other in the thermal equilibrium regime by the bidirectional ET.

The effective gain cross-section for a codoped material is:

$$\sigma_{g,eff} = \left(\beta_{Ho}\sigma_{SE,Ho} - (1-\beta_{Ho})\sigma_{abs,Ho}\right)\frac{N_{Ho}}{N_{tot}} + \left(\beta_{Tm}\sigma_{SE,Tm} - (1-\beta_{Tm})\sigma_{abs,Tm}\right)\frac{N_{Tm}}{N_{tot}}, \quad (6)$$

Here, the gain cross-section is defined with respect to the total (Tm + Ho) doping concentration of $N_{tot} = N_{Tm} + N_{Ho}$. Assuming population of only the ($^3H_6$, $^3F_4$) Tm^{3+} and ($^5I_8$, $^5I_7$) Ho^{3+} multiplets, the condition of the thermal equilibrium state established by the bidirectional $Tm^{3+} \leftrightarrow Ho^{3+}$ ET reads:

$$P_{28}(\mathrm{Tm} \rightarrow \mathrm{Ho}) \cdot N_2(^3F_4) \cdot \left(N_{Ho} - N_7(^5I_7)\right) = P_{71}(\mathrm{Ho} \rightarrow \mathrm{Tm}) \cdot N_7(^5I_7) \cdot \left(N_{Tm} - N_2(^3F_4)\right). \quad (7)$$

From Eq. (7), we arrive at:

$$\beta_{Ho} = \frac{\Omega\beta_{Tm}}{1+(\Omega-1)\beta_{Tm}}. \quad (8)$$

Here, $\Omega = 1/\Theta$ where Θ describes the rates of the direct and back ET, as described above.

The calculated $\sigma_{g,eff}$ spectra are shown in Figure 9 for different inversion rates for Tm^{3+} ions β_{Tm}. The gain spectra are smooth and broad. For small $\beta_{Tm} < 0.04$, the spectra are almost flat extending beyond 2.1 μm. With increasing inversion rate, the local maximum in the gain spectra experiences a blue-shift from ~2100 nm to 2081 nm. The local peak at 2081 nm due to the $^5I_7 \rightarrow {}^5I_8$ Ho^{3+} emission dominates the spectra for $\beta_{Tm} > 0.05$. At shorter wavelengths, the gain is first due to both Tm^{3+} and Ho^{3+} ions and then, below approximately 2 μm – mostly to the Tm^{3+} ions. For $\beta_{Tm} = 0.15$, the gain bandwidth (FWHM) $\Delta\lambda_g$ exceeds 150 nm.

5. Laser operation

5.2. Laser set-up: Diode-pumped laser

The diode-pumped laser performance of Tm,Ho:CNGG was studied in a simple plano-plano (microchip-type) laser cavity, Figure 10. The rectangular crystal with a thickness of 3.3 mm and an aperture of 3×3 mm^2 was wrapped in In-foil from all 4 lateral sides for better heat removal. It was fixed in a Cu-holder cooled by circulating water (12 °C). Both end-facets of the crystal were polished to laser quality and remained uncoated. The laser cavity was composed by a flat pump mirror (PM) coated for high transmission (HT) at ~0.80 μm (the pump wavelength) and for high reflection (HR) at 1.8-2.1 μm, and a set of flat output couplers (OCs) with measured transmission T_{OC} = 0.2%-9% at the laser wavelength. Both cavity mirrors were placed close to the crystal end-faces resulting in a geometrical cavity length of ~3.5 mm.

As a pump source, we employed a fiber-coupled (fiber core diameter: 200 μm, N.A. = 0.22) AlGaAs laser diode emitting unpolarized output at ~802 nm (M^2 >80, i.e., almost "top-hat" pump beam). The diode emission wavelength was stabilized by circulating water. The pump beam was collimated and focused into the crystal through the PM using an antireflection (AR) coated lens assembly (reimaging ratio: 1:1, focal length: f = 30 mm). The pump spot diameter in the focus was $2w_P$ = 200 μm and the confocal parameter was $2z_R$ = 1.8 mm. Pumping was realized in a double-pass configuration, as all the OCs provided partial reflection at the pump wavelength ($R \approx 40\%$). The double-pass absorption was calculated from pump-transmission measurements under non-lasing conditions at the threshold, η_{abs}(2-passes) = 43.8±0.5%.

The spectra of the laser emission were measured with a spectrum analyzer (WaveScan, 1000-2600 nm, APE GmbH) with a resolution of 0.2 nm.

5.2. Diode-pumped laser performance

The input-output characteristics of the CW diode-pumped Tm,Ho:CNGG laser are shown in Figure 11(a). The laser generated a maximum output power of 413 mW at 2088.4 nm with a slope efficiency η of 15.9% (vs. the absorbed pump power P_{abs}, fitting the linear part of the output dependence). The laser threshold was at P_{abs} = 0.37 W and the optical-to-optical laser efficiency η_{opt} was 5.3% (all the characteristics are specified for T_{OC} = 1.5%). The laser threshold gradually increased with output coupling, from 0.18 W (T_{OC} = 0.2%) up to 0.60 W (T_{OC} = 9%). For T_{OC} > 3%, the slope efficiency deteriorated which is common for Tm,Ho lasers and is related to enhanced upconversion in the gain medium causing more serious thermal

issues. A thermal roll-over in the output dependences was observed for $P_{abs} > 2.5$ W. Thus, the power scaling was limited by the risk of thermal fracture.

The laser emission was unpolarized. With increasing the output coupling, the laser spectra exhibited a blue-shift, from 2102.2 nm (T_{OC} = 0.2%) to 2069.8 nm (T_{OC} = 9%), Figure 11(b). This shift is related to the weaker reabsorption losses at high inversion levels β and is typical for quasi-three-level lasers. This spectral behavior is also in line with the gain spectra, Figure 9. The laser emission is related solely to Ho^{3+} ions (the $^5I_7 \rightarrow {}^5I_8$ transition).

5.3. Laser set-up: Mode-locked laser

A standard X-shaped cavity as shown in Figure 12 was employed to investigate the mode-locked laser performance of Tm,Ho:CNGG. The sample used had a size of 3×3×6 mm^3 with both end-faces (3×3 mm^2) antireflection (AR) coated for the wavelength ranges of 780-810 and 1800-2300 nm. To remove the generated heat during laser operation, it was tightly mounted in a Cu-holder which was water cooled to 14 °C. The laser element was placed at normal incidence between two folding concave mirrors M_1 and M_2 (radius of curvature, RoC = 100 mm) with a separation of ~108 mm. The pump source applied was a narrow-band CW Ti:Sapphire laser with a maximum output power of 3.6 W at 785.6 nm. The pump beam was focused into the laser crystal through the folding mirror M_1 using a focusing lens (focal length: f = 70 mm) resulting in a spot diameter $2w_P$ of ~60 µm (in the crystal). The calculated size of the laser mode in the crystal was 31 µm for both the tangential and sagittal planes. The crystal was pumped in a single-pass. The pump absorption under lasing conditions was weakly dependent on the pump level and output coupling and amounted to 61±1%.

For CW laser experiments, we used a flat highly-reflective mirror M_3 and a set of flat OCs with T_{OC} = 0.2%-3.0% at the laser wavelength. For the wavelength tuning experiment, a Lyot filter was inserted near the OC. The Lyot filter was a 3.2 mm-thick quartz plate with the optical axis at 60° to the surface. Finally, for ML operation, three chirped mirrors (Layertec GmbH), CM_1−CM_3, were employed for intracavity dispersion compensation, each of them providing a group delay dispersion, GDD = −125 fs^2 per bounce. The GaSb-based SESAM used as a saturable absorber exhibits an anti-resonant design at 2-µm wavelength and contained two quantum wells separated by 10 nm. The QWs are placed 50 nm below the surface, realized by a 50 nm thick GaSb cap layer. The measured relaxation time (slow component) for the uncoated SESAM amounted to 21 ps [35]. The flat highly-reflective mirror M_3 was replaced by a concave chirped mirror (CM_1), RoC = 100 mm) forming a waist on the SESAM. The

calculated mode radius at the SESAM was 107 and 105 μm in the tangential and sagittal planes, respectively.

The laser spectrum was measured using a spectrum analyzer (WaveScan, extended IR, APE GmbH), the radio frequency (RF) spectrum – by a fast InGaAs PIN photodiode (ET-50000, EOT Inc) and a RF spectrum analyzer (R&S FSP7, Rohde&Schwarz), and the autocorrelation (AC) trace - by a commercial autocorrelator (pulseCheck, APE GmbH).

5.4. CW wavelength tuning

With the highly-reflective mirror M_3 and without the Lyot filter, the laser operated in CW (free-running) regime, Figure 13(a,b). It generated 425 mW at 2083.7 nm with η = 22.9% (for T_{OC} = 3.0%). The laser threshold slightly increased with the output coupling, from P_{abs} = 80 mW (T_{OC} = 0.2%) to 136 mW (T_{OC} = 3.0%). The output dependences were linear and the power scaling was limited by the available pump. Lower threshold as compared to diode pumping is explained by the better quality of the pump beam. The somewhat better slope efficiency is probably due to the better mode-matching. The laser wavelength experienced a blue-shift with increasing T_{OC}, from 2097.4 and 2099.4 nm (T_{OC} = 0.2%) to 2083.7 nm (T_{OC} = 3.0%), the same behaviour as in the case of diode-pumping and agrees with the gain spectra.

Wavelength tuning of the Tm,Ho:CNGG laser was studied by inserting the Lyot filter into the cavity, close to the OC. The tuning performance was characterized with the 0.2% and 0.5% OCs. A continuous tuning of the emission wavelength from 1932.5 to 2142.1 nm (T_{OC} = 0.5%) and from 1940.3 to 2144.6 nm (T_{OC} = 0.2%) was achieved, equivalent to >200 nm tuning range in both cases (determined at the zero power level). This highlights the suitability of the Tm,Ho:CNGG disordered crystal for the generation of ultrashort laser pulses. The maximum in the tuning curves was observed at ~2088 nm.

The effective gain cross-section, $\sigma_{g,eff}$, spectra for Tm,Ho:CNGG were calculated to explain the observed wavelength tuning performance, Figure 13(c). For the calculation, we used β_{Tm} = 0.11, so that, according to Eq. (8), β_{Ho} = 0.52. The gain spectrum reasonably agrees with the measured wavelength tunability curve. In the same graph, we show the gain spectrum for Ho^{3+} ions only, $\sigma_{g,Ho}$. It is narrower and cannot explain the wavelength tuning below 2 μm. Thus, both Ho^{3+} and Tm^{3+} ions contribute to the observed tuning range.

In a previous work on Tm^{3+},Na^{+}:CNGG [12], a tuning range of 168 nm (1885-2053 nm) was achieved. Thus, Tm^{3+},Ho^{3+} codoping extends this range to well beyond 2 μm when using CNGG as host.

5.5. Femtosecond mode-locked laser operation

The ML performance was studied with the CMs and the GaSb based SESAM inserted into the cavity, leading to a total physical cavity length of about 1.68 m. Considering the group velocity dispersion of the laser crystal, approximately −31 fs^2/mm at ~2.06 μm, the total round-trip GDD amounted to −1622 fs^2. ML operation was first achieved by employing the 1.5% OC. The absorbed pump power was set at P_{abs} = 2.0 W. After carefully optimizing the separations of M_1-M_2 and CM_3-SESAM, and adjusting the position of the SESAM and the Tm,Ho:CNGG crystal, stable and self-starting ML operation was obtained. Pulses as short as 100 fs were generated without external compression. The corresponding autocorrelation trace and optical spectrum were measured, see Figure 14(a,b). The emission spectrum was centered at 2067 nm and had a FWHM of 45.3 nm. This leads to a time-bandwidth product (TBP) of 0.318, corresponding to nearly Fourier-limited pulses. The measured average output power of the mode-locked laser was 105 mW.

With the aim to achieve shorter pulses, an OC with lower transmission, T_{OC} = 0.5%, was employed. As expected, shorter pulses were obtained and its duration amounted to 73 fs without external compression. The corresponding autocorrelation trace and optical spectrum are shown in Figure 14(c,d). The spectrum was centered at 2061 nm and had a FWHM of 61.5 nm. This leads to a TBP of 0.317, again corresponding to nearly Fourier-limited pulses. The measured average output power of the mode-locked laser was lower compared to the performance with the 1.5% OC, 36 mW, under the same P_{abs}.

The stability of the ML regime of operation was assessed by measurements with a RF spectrum analyzer. The RF spectrum shows an extinction ratio above the noise level of ~81 dB for the fundamental beat note, measured with a resolution bandwidth (RBW) of 100 Hz, Figure 15(a). The uniform harmonic beat notes recorded in Figure 15(b) indicate stable mode-locking without any Q-switching or other instabilities. The pulse repetition rate of ~89.3 MHz corresponds to the cavity length of ~1.68 m. The results were similar for the two studied OCs.

The obtained pulses are shorter than in the previous work with the Tm,Ho:CNGG crystal [22] where a SWCNT saturable absorber was employed: Pan *et al.* reported on 83 fs pulses at 2081 nm (emission bandwidth: 57.5 nm). This shortening is probably due to the better matching of the pump and laser modes for the designed cavity employing an AR-coated laser crystal placed at normal incidence (in [22], the crystal was placed at the Brewster angle).

6. Conclusions

To conclude, Tm^{3+},Ho^{3+}-codoped disordered CNGG garnet is an attractive material for broadly tunable and sub-100 fs mode-locked lasers emitting slightly above 2 μm owing to its attractive spectroscopic properties, i.e., (i) inhomogeneously broadened and smooth emission spectra at ~2 μm, (ii) efficient and predominantly unidirectional (direct) $Tm^{3+} \rightarrow Ho^{3+}$ energy transfer, as expressed by the equilibrium constant $\Theta = P_{71}/P_{28} = 0.115$, (iii) a relatively long lifetime of the Ho^{3+} upper laser level (8.41 ms, radiative) and the thermal equilibrium lifetime for the Tm^{3+},Ho^{3+} system (6.80 ms, measured) leading to a relatively low laser threshold, and (iv) the contribution of both Tm^{3+} and Ho^{3+} ions to the gain spectra featuring a bandwidth of more than 150 nm. We report on the first diode-pumped laser operation of Tm,Ho:CNGG yielding 413 mW at 2088.4 nm with a slope efficiency of 15.9%. A tuning range of ~200 nm (with the laser wavelength up to 2144.6 nm) is demonstrated for this crystal. Finally, when employing a GaSb SESAM, sub-100 fs nearly Fourier-limited pulses (73 fs, without external compression) are generated.

Further work with Tm,Ho:CNGG crystals should focus on their codoping by univalent alkali metal cations (Na^+, Li^+ or their combination) serving two aims: (i) elimination of the unwanted cationic vacancies and (ii) possible further extension of the gain bandwidth.

Acknowledgements

This work was supported by the Spanish Government (project No. MAT2016-75716-C2-1-R (AEI/FEDER,UE)), Catalan Government (project No. 2017SGR755), Foundation of the President of China Academy of Engineering Physics (project No. YZJJLX2018005), National Natural Science Foundation of China (projects No. 61975208, 51761135115 and 61875199), Fund of Key Laboratory of Optoelectronic Materials Chemistry and Physics, Chinese Academy of Sciences (project No. 2008DP173016) and Deutsche Forschungsgemeinschaft (project No. PE 607/14-1).

References

1. Yu. K. Voronko, A. A. Sobol, A. Y. Karasik, N. A. Eskov, P. A. Rabochkina, S. N. Ushakov, Calcium niobium gallium and calcium lithium niobium gallium garnets doped with rare earth ions – effective laser media, Opt. Mater. 20 (2002) 197-209.

2. K. Shimamura, M. Timoshechkin, T. Sasaki, K. Hoshikawa, T. Fukuda, Growth and characterization of calcium niobium gallium garnet (CNGG) single crystals for laser applications, J. Cryst. Growth 128 (1993) 1021-1024.

3. E. Castellano-Hernández, M. D. Serrano, R. J. Jiménez Riobóo, C. Cascales, C. Zaldo, A. Jezowski, P. A. Loiko, Na modification of lanthanide doped $Ca_3Nb_{1.5}Ga_{3.5}O_{12}$-type laser garnets: Czochralski crystal growth and characterization, Cryst. Growth Des. 16 (2016) 1480-1491.
4. A. Lupei, V. Lupei, L. Gheorghe, L. Rogobete, E. Osiac, A. Petraru, The nature of nonequivalent Nd^{3+} centers in CNGG and CLNGG, Opt. Mater. 16 (2001) 403-411.
5. A. Schmidt, U. Griebner, H. Zhang, J. Wang, M. Jiang, J. Liu, V. Petrov, Passive mode-locking of the Yb:CNGG laser, Opt. Commun. 283 (2010) 567-569.
6. Y. G. Zhang, V. Petrov, U. Griebner, X. Zhang, H. H. Yu, H. J. Zhang, J. H. Liu, Diode-pumped SESAM mode-locked Yb:CLNGG laser, Opt. Laser Technol. 69 (2015) 144–147.
7. G. Q. Xie, L. J. Qian, P. Yuan, D. Y. Tang, W. D. Tan, H. H. Yu, H. J. Zhang, J. Y. Wang, Generation of 534 fs pulses from a passively mode-locked Nd:CLNGG-CNGG disordered crystal hybrid laser, Laser Phys. Lett. 7 (2010) 483-486.
8. J. Ma, Z. Pan, J. Wang, H. Yuan, H. Cai, G. Xie, L. Qian, D. Shen, D. Tang, Generation of sub-50 fs soliton pulses from a mode-locked Yb,Na:CNGG disordered crystal laser, Opt. Express 25 (2017) 14968-14973.
9. V. Petrov, Frequency down-conversion of solid-state laser sources to the mid-infrared spectral range using non-oxide nonlinear crystals, Prog. Quantum Electron. 42 (2015) 1-106.
10. Y. K. Voronko, S. B. Gessen, N. A. Es'kov, P. A. Ryabochkina, A. A. Sobol, S. N. Ushakov, L. I. Tsymbal, Lasing and spectroscopic properties of calcium-niobium-gallium garnet crystals doped with Tm^{3+} ions, Quantum Electron. 23 (1993) 309-311.
11. Y. K. Voronko, S. B. Gessen, N. A. Es'kov, A. A. Kiryukhin, P. A. Ryabochkina, A. A. Sobol, V. M. Tatarintsev, S. N. Ushakov, L. I. Tsymbal, Interaction of Tm^{3+} ions in calcium-niobium-gallium and yttrium-aluminum garnet laser crystals, Quantum Electron. 23 (1993) 958-961.
12. Z. Pan, J. M. Serres, E. Kifle, P. Loiko, H. Yuan, X. Dai, H. Cai, M. Aguiló, F. Díaz, Y. Wang, Y. Zhao, U. Griebner, V. Petrov, X. Mateos, Comparative study of the spectroscopic and laser properties of Tm^{3+}, $Na^{+}(Li^{+})$-codoped $Ca_3Nb_{1.5}Ga_{3.5}O_{12}$-type disordered garnet crystals for mode-locked lasers, Opt. Mater. Express 8 (2018) 2287-2299.
13. Y. Wang, Y. Zhao, Z. Pan, J. E. Bae, S. Y. Choi, F. Rotermund, P. Loiko, J. M. Serres, X. Mateos, H. Yu, H. Zhang, M. Mero, U. Griebner, V. Petrov, 78 fs SWCNT-SA mode-locked Tm:CLNGG disordered garnet crystal laser at 2017 nm, Opt. Lett. 43 (2018) 4268-4271.

14. Z. Pan, Y. Wang, Y. Zhao, H. Yuan, X. Dai, H. Cai, J. E. Bae, S. Y. Choi, F. Rotermund, X. Mateos, J. M. Serres, P. Loiko, U. Griebner, V. Petrov, Generation of 84-fs pulses from a mode-locked Tm:CNNGG disordered garnet crystal laser, Photon. Res. 6 (2018) 800-804.
15. Y. Wang, G. Xie, X. Xu, J. Di, Z. Qin, S. Suomalainen, M. Guina, A. Härkönen, A. Agnesi, U. Griebner, X. Mateos, P. Loiko, V. Petrov, SESAM mode-locked Tm:CALGO laser at 2 μm, Opt. Mater. Express 6 (2016) 131-136.
16. P. Loiko, J.M. Serres, X. Mateos, K. Yumashev, N. Kuleshov, V. Petrov, U. Griebner, M. Aguiló, F. Díaz, In-band-pumped Ho:$KLu(WO_4)_2$ microchip laser with 84% slope efficiency, Opt. Lett. 40 (2015) 344-347.
17. S. Lamrini, P. Koopmann, M. Schäfer, K. Scholle, P. Fuhrberg, Efficient high-power Ho:YAG laser directly in-band pumped by a GaSb-based laser diode stack at 1.9 μm, Appl. Phys. B 106 (2012) 315-319.
18. P. Loiko, J. M. Serres, X. Mateos, K. Yumashev, N. Kuleshov, V. Petrov, U. Griebner, M. Aguiló, F. Díaz, Microchip laser operation of Tm,Ho:$KLu(WO_4)_2$ crystal, Opt. Express 22 (2014) 27976-27984.
19. Y. Zhao, Y. Wang, X. Zhang, X. Mateos, Z. Pan, P. Loiko, W. Zhou, X. Xu, J. Xu, D. Shen, S. Suomalainen, A. Härkönen, M. Guina, U. Griebner, V. Petrov, 87 fs mode-locked Tm,Ho:$CaYAlO_4$ laser at ~2043 nm, Opt. Lett. 43 (2018) 915-918.
20. P. A. Ryabochkina, A. N. Chabushkin, N. G. E. Zakharov, K. V. E. Vorontsov, S. A. Khrushchalina, Tunable 2-μm lasing in calcium–niobium–gallium garnet crystals doped with Ho^{3+} ions, Quantum Electron. 47 (2017) 607-609.
21. Y. Xue, N. Li, Q. Song, X. Xu, X. Yang, T. Dai, D. Wang, Q. Wang, D. Li, Z. Wang, J. Xu, Spectral properties and laser performance of Ho:CNGG crystals grown by the micro-pulling-down method, Opt. Mater. Express 9 (2019) 2490-2496.
22. Z. Pan, Y. Wang, Y. Zhao, M. Kowalczyk, J. Sotor, H. Yuan, Y. Zhang, X. Dai, H. Cai, J. E. Bae, S. Y. Choi, F. Rotermund, P. Loiko, J. M. Serres, X. Mateos, U. Griebner, V. Petrov, Sub-80 fs mode-locked Tm,Ho-codoped disordered garnet crystal oscillator operating at 2081 nm, Opt. Lett. 43 (2018) 5154-5157.
23. G. A. Novak, G. V. Gibbs, The crystal chemistry of the silicate garnets, Amer. Mineral. 56 (1971) 791-825.
24. M. D. Serrano, J. O. Álvarez-Pérez, C. Zaldo, J. Sanz, I. Sobrados, J. A. Alonso, C. Cascales, M. T. Fernández-Díaz, A. Jezowski, Design of Yb^{3+} optical bandwidths by crystallographic modification of disordered calcium niobium gallium laser garnets, J. Mater. Chem. C 5 (2017) 11481-11495.

25. R. D. Shannon, Revised effective ionic radii and systematic studies of interatomic distances in halides and chalcogenides, Acta Cryst. A 32 (1976) 751-767.
26. Y. Ono, K. Shimamura, Y. Morii, T. Fukuda, T. Kajitani, Structure analysis of a CaNbGa garnet, Phys. B: Cond. Matter 213 (1995) 420-422.
27. W. T. Carnall, P. R. Fields, K. Rajnak, Electronic energy levels in the trivalent lanthanide aquo ions. I. Pr^{3+}, Nd^{3+}, Pm^{3+}, Sm^{3+}, Dy^{3+}, Ho^{3+}, Er^{3+}, and Tm^{3+}, J. Chem. Phys. 49 (1968) 4424-4442.
28. B. R. Judd, Optical absorption intensities of rare-earth ions, Phys. Rev. 127 (1962) 750-761.
29. G. S. Ofelt, Intensities of crystal spectra of rare-earth ions, J. Chem. Phys. 37 (1962) 511-520.
30. A. A. Kornienko, A.A. Kaminskii, E. B. Dunina, Dependence of the line strength of f–f transitions on the manifold energy. II. Analysis of Pr^{3+} in $KPrP_4O_{12}$, Phys. Status Solidi B 157 (1990) 267-273.
31. P. Loiko, A. Volokitina, X. Mateos, E. Dunina, A. Kornienko, E. Vilejshikova, M. Aguiló, F. Díaz, Spectroscopy of Tb^{3+} ions in monoclinic $KLu(WO_4)_2$ crystal: Application of an intermediate configuration interaction theory, Opt. Mater. 78 (2018) 495-501.
32. L. Zhang, P. Loiko, J.M. Serres, E. Kifle, H. Lin, G. Zhang, E. Vilejshikova, E. Dunina, A. Kornienko, L. Fomicheva, U. Griebner, V. Petrov, Z. Lin, W. Chen, K. Subbotin, M. Aguiló, F. Díaz, X. Mateos, Growth, spectroscopy and first laser operation of monoclinic Ho^{3+}:$MgWO_4$ crystal, J. Lumin. 213 (2019) 316-325.
33. B. M. Walsh, N. P. Barnes, B. Di Bartolo, The temperature dependence of energy transfer between the Tm $^3F_4$ and Ho $^5I_7$ manifolds of Tm-sensitized Ho luminescence in YAG and YLF, J. Lumin. 90 (2000) 39-48.
34. B. Aull, H. Jenssen, Vibronic interactions in Nd:YAG resulting in nonreciprocity of absorption and stimulated emission cross sections, IEEE J. Quantum Electron. 18 (1982) 925-930.
35. J. Paajaste, S. Suomalainen, A. Härkönen, U. Griebner, G. Steinmeyer, M. Guina, Absorption recovery dynamics in 2 μm GaSb-based SESAMs, J. Phys D 46 (2014) 065102-1-6.

List of figure captions

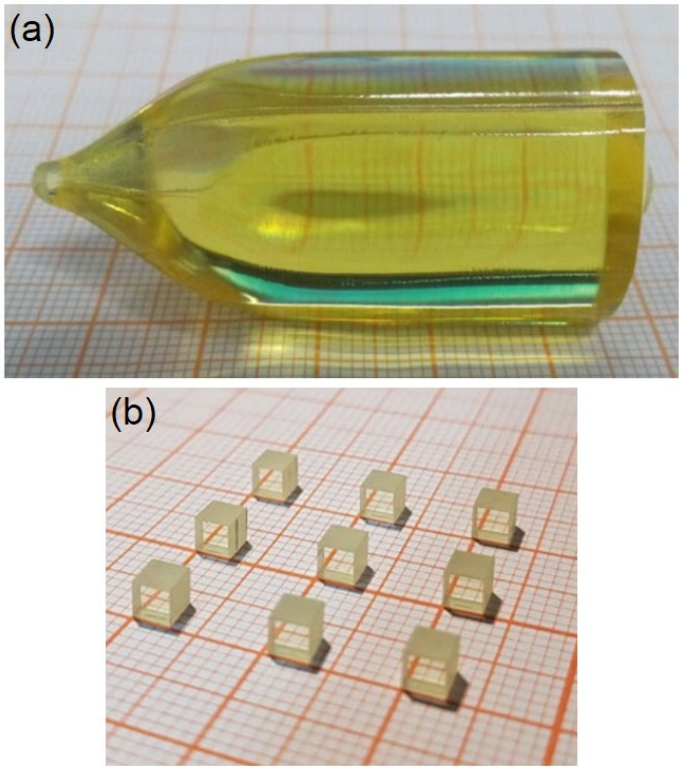

Figure 1. (a) Photograph of the as-grown 2.64 at.% Tm, 0.55 at.% Ho:CNGG crystal, the growth direction is along the [111] axis; (b) polished laser elements fabricated from the crystal boule which are annealed in air at 1373 K.

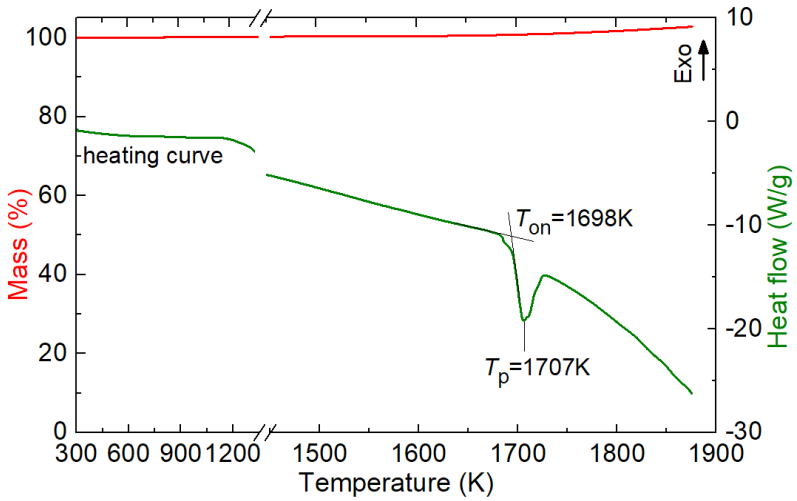

Figure 2. TG-DSC curve of the Tm,Ho:CNGG crystal.

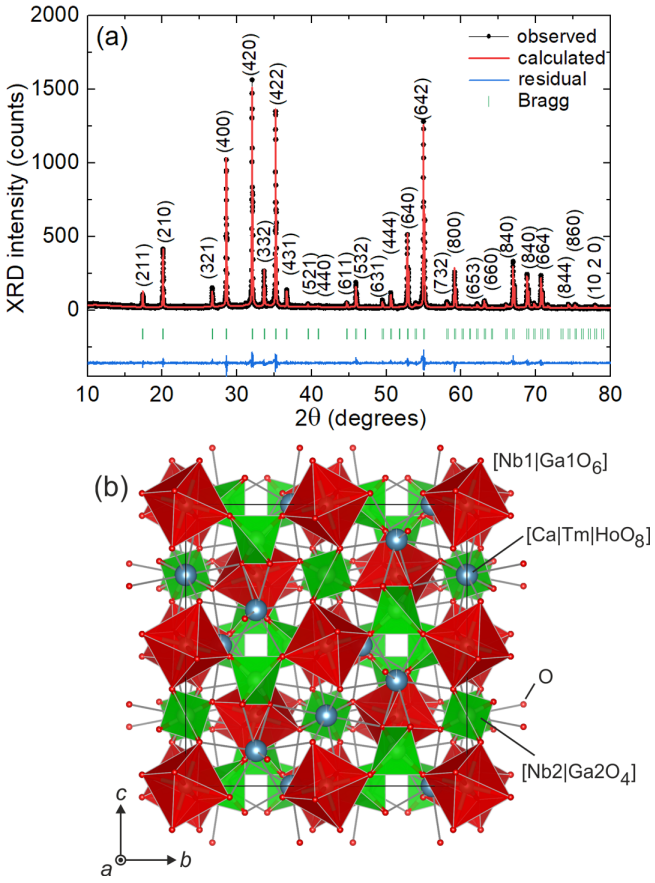

Figure 3. (a) X-ray powder diffraction (XRD) pattern of the 2.64 at.% Tm, 0.55 at.% Ho:CNGG crystal showing the results of the Rietveld refinement, numbers denote the Miller's indices (*hkl*); (b) fragment of crystal structure in projection on the ***b*-*c*** plane.

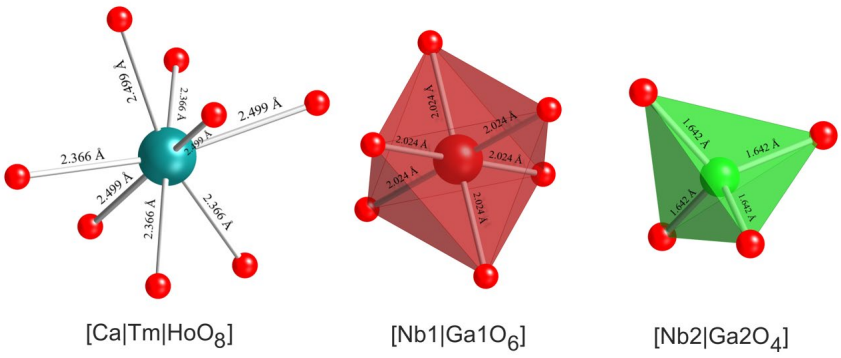

Figure 4. Oxygen coordination and metal – oxygen interatomic distances for the dodecahedral sites (Ca|Tm|Ho), octahedral sites (Nb1|Ga1) and tetrahedral sites (Nb2|Ga2) in the Tm,Ho:CNGG garnet.

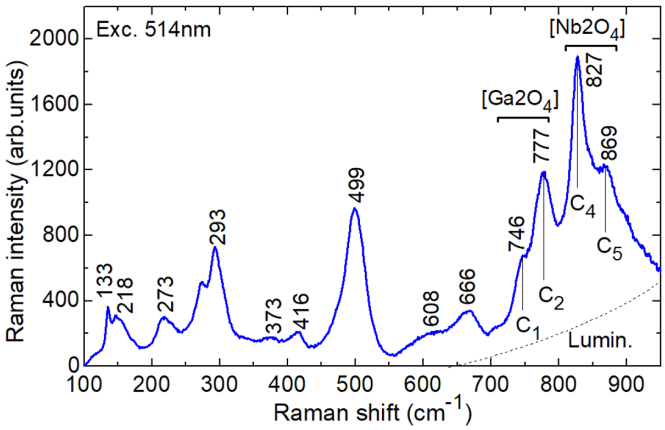

Figure 5. Unpolarized Raman spectrum of the Tm,Ho:CNGG crystal, λ_{exc} = 514 nm. *Numbers* indicate the Raman energy in cm^{-1}. C_i are the bands due to symmetric stretching vibrations in $[M2O_4]$ (M2 = Ga2|Nb2) tetrahedra; *Dashed line* – luminescence background.

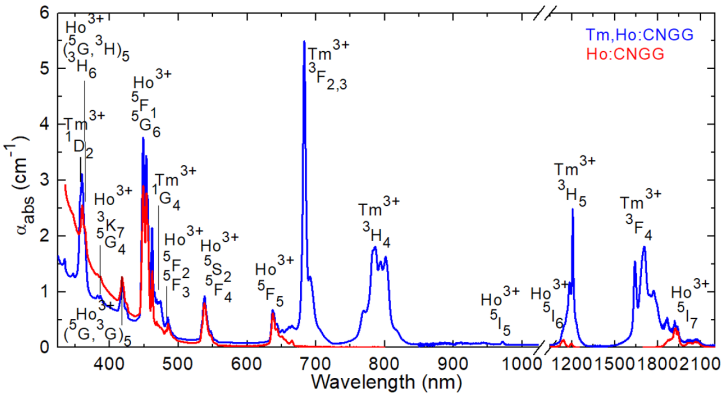

Figure 6. Absorption spectra of 2.64 at.% Tm, 0.55 at.% Ho:CNGG and 0.55 at.% Ho:CNGG.

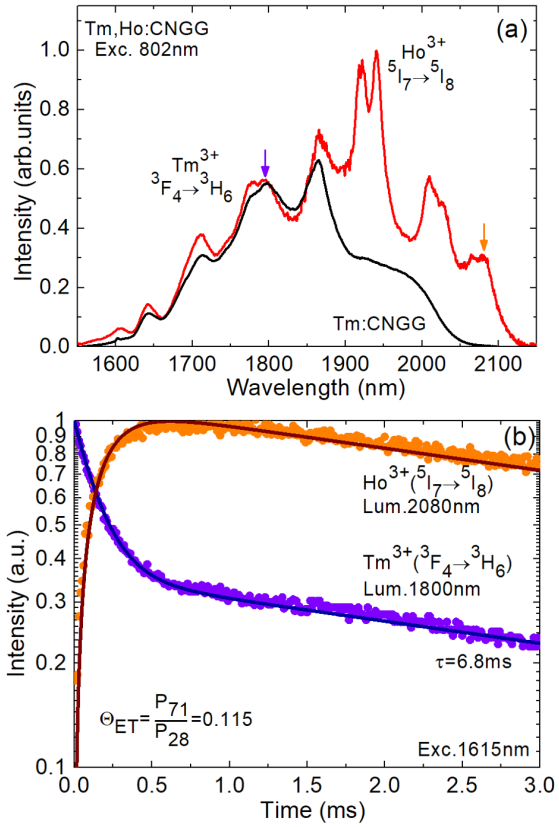

Figure 7. (a) Luminescence spectrum of the Tm,Ho:CNGG crystal at ~2 μm, λ_{exc} = 802 nm. The spectrum of singly-doped Tm:CNGG crystal is given for comparison. The *arrows* indicate the wavelength selected for the decay studies; (b) luminescence decay curves for the Tm,Ho:CNGG crystal measured at 2080 nm (Ho^{3+} emission) and at 1800 nm (Tm^{3+} emission), λ_{exc} = 1615 nm: *symbols* – experimental data, *curves* – their modeling with Eq. (3).

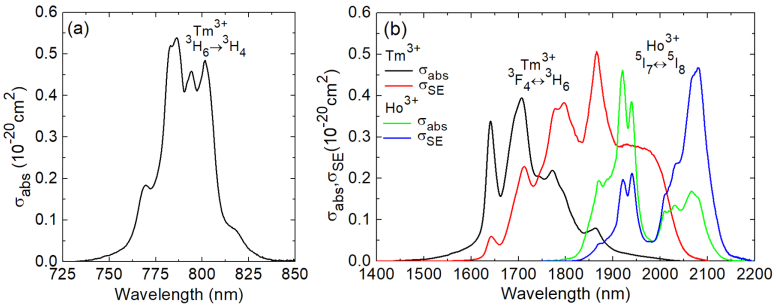

Figure 8. Spectroscopy of Tm^{3+} and Ho^{3+} ions in CNGG: (a) absorption cross-section, σ_{abs}, for the $^3H_6 \rightarrow {}^3H_4$ Tm^{3+} transition; (b) absorption, σ_{abs}, and stimulated-emission (SE), σ_{SE}, cross-sections for the $^3F_4 \leftrightarrow {}^3H_6$ Tm^{3+} and $^5I_7 \leftrightarrow {}^5I_8$ Ho^{3+} transitions.

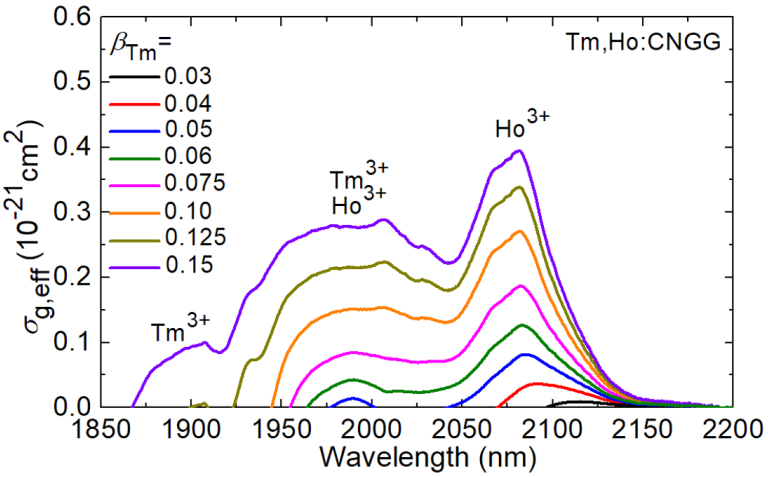

Figure 9. Effective gain cross-sections, $\sigma_{g,eff}$, for the 2.64 at.% Tm, 0.55 at.% Ho:CNGG at ~2 μm: $\beta_{Tm} = N_2(^3F_4)/N_{Tm}$ is the inversion level for Tm^{3+} ions; calculated using Eqs. (6)-(8).

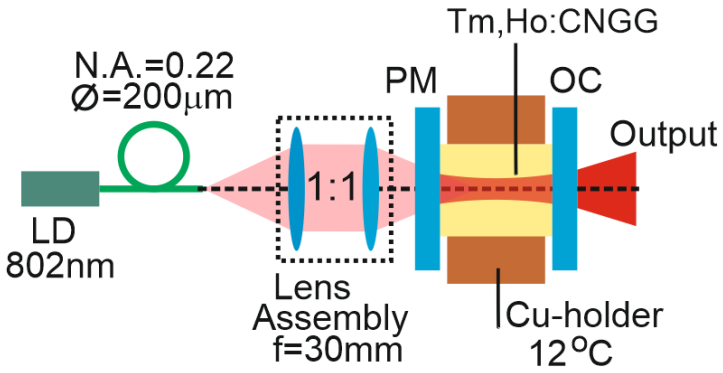

Figure 10. Scheme of the CW diode-pumped Tm,Ho:CNGG laser: LD – laser diode, PM – pump mirror, OC – output coupler.

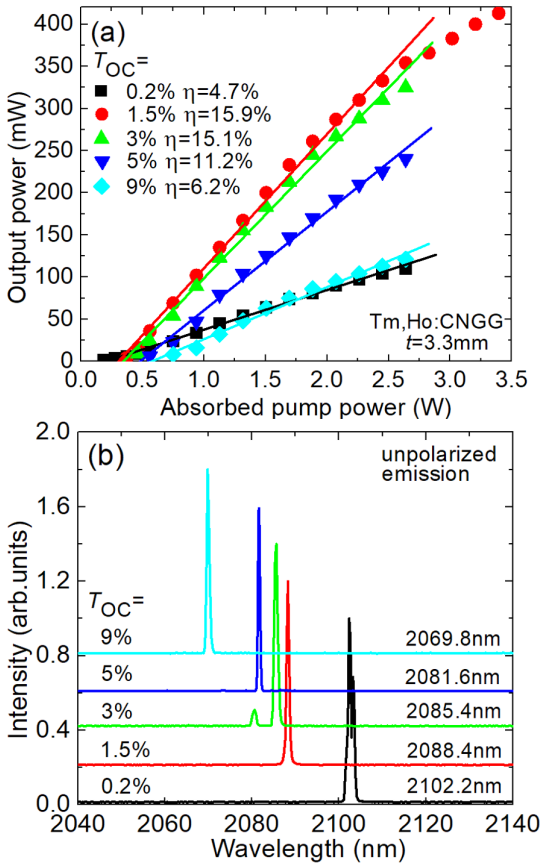

Figure 11. Continuous-wave diode-pumped Tm,Ho:CNGG laser: (a) input-output dependences, η – slope efficiency; (b) typical laser emission spectra measured at maximum P_{abs}.

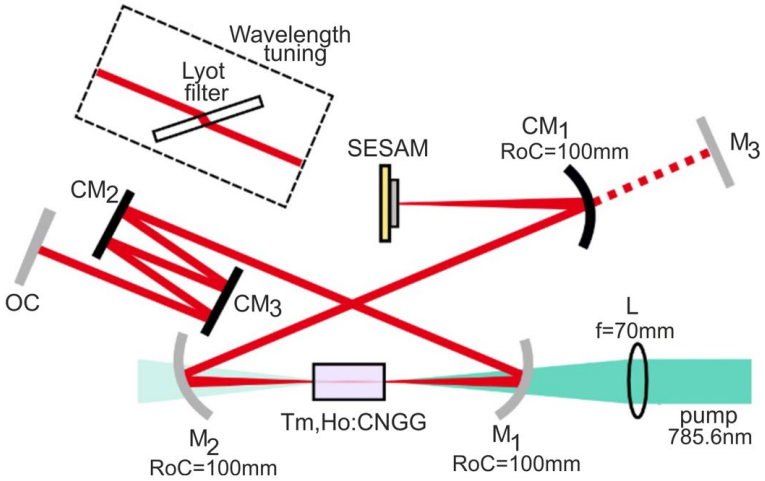

Figure 12. Layout of the mode-locked Tm,Ho:CNGG laser (L: lens; M_1 and M_2: dichroic folding mirrors; M_3: plane highly-reflective mirror; CM_1, CM_2 and CM_3: chirped mirrors; OC: output coupler).

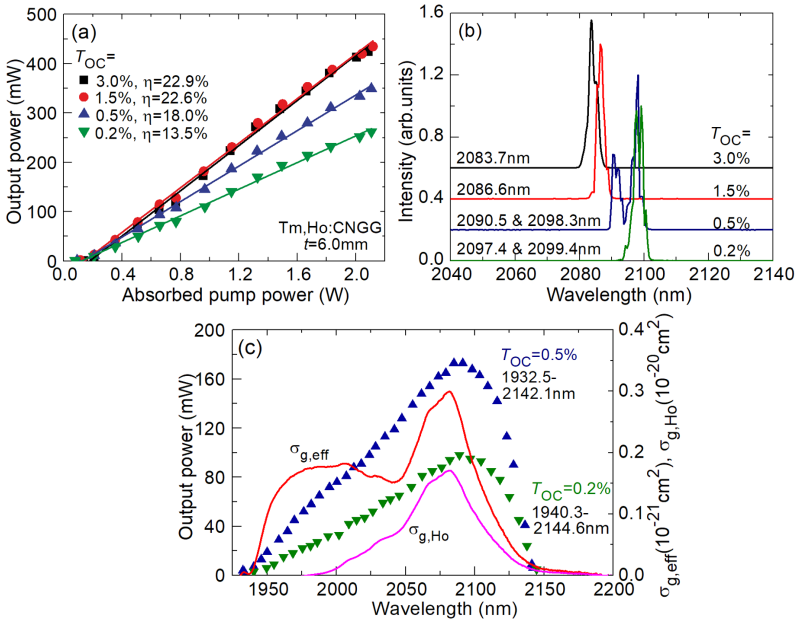

Figure 13. CW laser performance of the Tm,Ho:CNGG laser pumped by a Ti:Sapphire laser at 785.6 nm: (a,b) free-running operation, (a) input-output dependences, η – slope efficiency; (b) typical laser emission spectra measured at P_{abs} = 2.0 W; (c) *symbols*: wavelength tuning for T_{OC} = 0.2% and 0.5%, *curves*: calculated effective gain, $\sigma_{g,eff}$, Eq. (6), and Ho^{3+} gain, $\sigma_{g,Ho}$, Eq. (5), spectra for β_{Tm} = 0.11 and β_{Ho} = 0.52. The laser emission is linearly polarized.

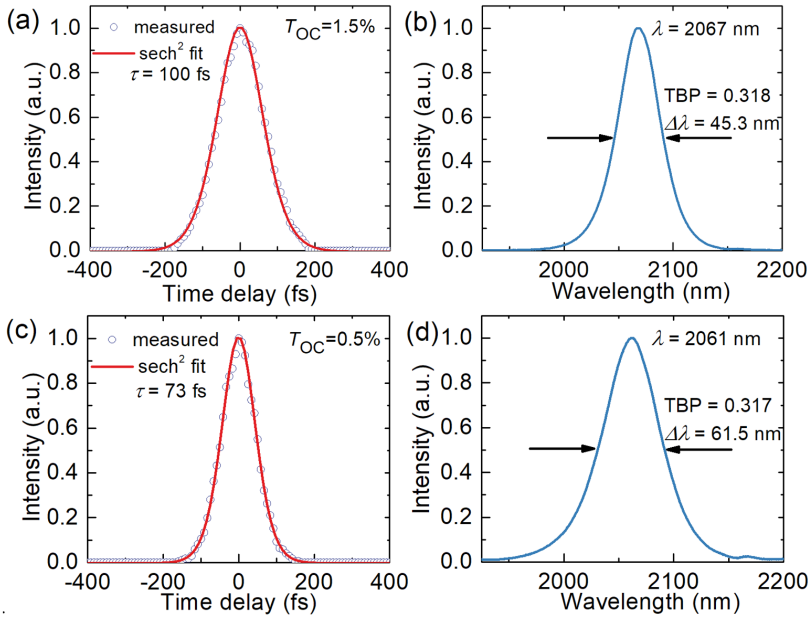

Figure 14. SESAM mode-locked Tm,Ho:CNGG laser: (a,c) autocorrelation traces (*symbols* - measured data, *red curves* - their $sech^2$ fits) and (b,d) corresponding spectra of the laser emission. (a,b) T_{OC} = 1.5%, (c,d) T_{OC} = 0.5%. P_{abs} = 2.0 W.

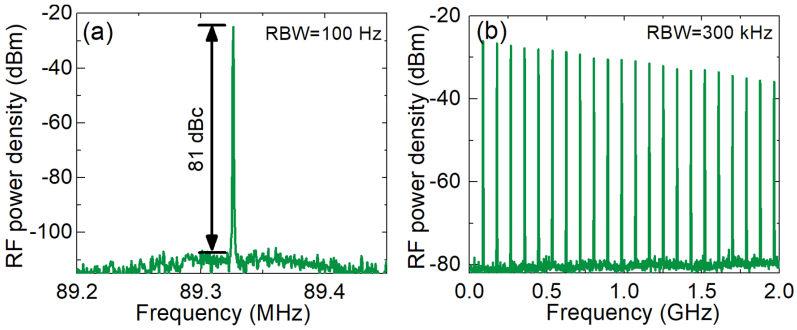

Figure 15. Radio frequency (RF) spectra of the SESAM mode-locked Tm,Ho:CNGG laser: (a) fundamental beat note and (b) 2.0 GHz wide span (RBW: resolution bandwidth). T_{OC} = 0.5%. P_{abs} = 2.0 W.

List of Tables

Table 1. Crystallographic data and structure refinement parameters for Tm,Ho:CNGG.

Parameters	Values
Chemical formula	$Ca_{2.895}Tm_{0.09}Ho_{0.015}Nb_{1.628}Ga_{3.25}O_{12}$
System	cubic
Space group	*I a* -3 *d*
Space group IT number	230
Lattice constants,	12.4952(1)
$a = b = c$ (Å)	
$\alpha = \beta = \gamma$ (deg.)	90
Unit-cell volume V (Å^3)	1950.87
2θ range (deg.)	10 - 80
Radiation	Cu Ka1 (λ = 1.5418 Å)
Calculated density (g/cm^3)	5.063
Refinement	Rietveld refinement with FULLPROF software
Reliability factors	R_p = 5.80, R_{wp} = 7.76, R_{exp} = 6.13 and χ^2 =1.60

Table 2. Fractional atomic coordinates (x, y, z), occupancy factors (O.F.) and isotropic displacement parameters (B_{iso}) for the Tm,Ho:CNGG crystal.

Atom	Wyckoff symbol	x	y	z	O.F.	B_{iso}, Å^2
Ca	24*c*	0.1250	0	0.2500	0.9681	1.22(3)
Tm	24*c*	0.1250	0	0.2500	0.0264	1.22(3)
Ho	24*c*	0.1250	0	0.2500	0.0055	1.22(3)
Ga1	16*a*	0	0	0	0.2900	0.98(1)
Nb1	16*a*	0	0	0	0.7100	0.98(1)
Nb2	24*d*	0.3750	0	0.2500	0.0820	0.75(1)
Ga2	24*d*	0.3750	0	0.2500	0.9180	0.75(1)
O	96*h*	0.0398	0.0488	0.6555	1	1.08(3)

Table 3. Bond lengths and geometric parameters of the [MO_n] polyhedrons in Tm,Ho:CNGG.

Parameter	Polyhedron		
	[Ca|Tm|HoO_8]	[Nb1|$Ga1O_6$]	[Nb2|$Ga2O_4$]
Bonds length M-O (Å)	2.4991(0) ×4	2.0242(1) ×6	1.6423(7) ×4
	2.3662(3) ×4	-	-
Average bond length (Å)	2.43270	2.0238	1.6425
Polyhedral volume (Å^3)	24.5481	11.046	2.2504
Distortion index (bond length)	0.02762	0.0	0.0
Quadratic elongation	-	1.0004	1.0071
Bond angle variance (deg.^{2})	-	1.3591	28.636
Effective coordination number	7.76	6.00	4.00

Table 4. Measured and calculated absorption oscillator strengths of the Ho^{3+} ion in CNGG[a].

Transition $^5I_8 \rightarrow {}^{2S'+1}L'_{J'}$	$\langle E_{J'} \rangle$, cm^{-1}	Γ, $cm^{-1}nm$	$f^{\Sigma}_{exp} \times 10^6$	$f^{\Sigma}_{calc} \times 10^6$ J–O	$f^{\Sigma}_{calc} \times 10^6$ ICI
$^5I_7$	5092	35.618	1.563	1.715^{ED}+ 0.580^{MD}	1.037^{ED}+ 0.580^{MD}
$^5I_6$	8658	6.597	0.834	1.196^{ED}	0.955^{ED}
$^5F_5$	15414	8.977	3.608	4.790^{ED}	3.671^{ED}
$^5S_2 + {}^5F_4$	18531	9.738	5.584	5.360^{ED}	5.363^{ED}
$^5F_3$	20497	3.484	2.467	1.273^{ED}	1.649^{ED}
$^5F_{1,2} + {}^3K_8$ + $^5G_6$	21980	32.779	26.799	28.043^{ED}+ 0.132^{MD}	26.653^{ED}+ 0.132^{MD}
$^3G_5$	24060	5.582	5.360	6.624^{ED}	5.448^{ED}
$^5G2_5 + {}^3H_6$	27607	11.790	15.138	9.648^{ED}	15.096^{ED}
rms dev.				*2.784*	*1.260*

[a]$\langle E_{J'} \rangle$ - energy of the "center of gravity" of the absorption band, Γ – integrated absorption coefficient, f^{Σ}_{exp} and f^{Σ}_{calc} – experimental and calculated absorption oscillator strengths, respectively, ED and MD stand for the electric-dipole and magnetic-dipole contributions, respectively.

Table 5. Intensity parameters of the Ho^{3+} ion in CNGG.

Parameter	J-O theory	ICI theory
$\Omega_2 \times 10^{20}$, cm^2	4.107	11.132
$\Omega_4 \times 10^{20}$, cm^2	3.977	3.901
$\Omega_6 \times 10^{20}$, cm^2	1.383	2.179
$R_2 \times 10^4$, cm	-	0.398
$R_4 \times 10^4$, cm	-	0.136
$R_6 \times 10^4$, cm	-	0.093

Table 6. Calculated probabilities of spontaneous radiative transitions of the Ho^{3+} ion in CNGG[a].

Emitting state	Terminal state	‹λ›, nm	A^{Σ}_{calc}(JJ'), s^{-1}	B(JJ'), %	A_{tot}, s^{-1}	τ_{rad}, ms
$^5I_7$	$^5I_8$	1964	$76.3^{ED}+42.6^{MD}$	1	118.9	8.41
$^5I_6$	$^5I_7$	2804	$29.0^{ED}+24.3^{MD}$	0.183	291.6	3.43
	$^5I_8$	1155	238.3^{ED}	0.817		
$^5I_5$	$^5I_6$	3820	$10.7^{ED}+8.8^{MD}$	0.072	271.3	3.69
	$^5I_7$	1617	149.5^{ED}	0.551		
	$^5I_8$	886.8	102.4^{ED}	0.377		
$^5I_4$	$^5I_5$	4833	$11.7^{ED}+4.4^{MD}$	0.088	184.3	5.42
	$^5I_6$	2134	67.7^{ED}	0.367		
	$^5I_7$	1211	84.0^{ED}	0.456		
	$^5I_8$	749.3	16.5^{ED}	0.089		
$^5F_5$	$^5I_4$	4824	$0.15^{ED}+0.03^{MD}$	<0.001	4735.5	0.21
	$^5I_5$	2414	$18.4^{ED}+0.9^{MD}$	0.004		
	$^5I_6$	1479	$208.4^{ED}+2.8^{MD}$	0.044		
	$^5I_7$	968.4	964.7^{ED}	0.204		
	$^5I_8$	648.6	3540.2^{ED}	0.748		
$^5S_2+^5F_4$	$^5F_5$	3212	$66.9^{ED}+8.2^{MD}$	0.005	15698	0.064
	$^5I_4$	1928	$179.0^{ED}+0.08^{MD}$	0.011		
	$^5I_5$	1378	$488.4^{ED}+0.3^{MD}$	0.031		
	$^5I_6$	1013	1162.6^{ED}	0.074		
	$^5I_7$	744.1	3138.0^{ED}	0.200		
	$^5I_8$	539.6	10654^{ED}	0.679		

[a]‹λ› - mean wavelength of the emission band, $A^{\Sigma}_{calc}(JJ')$ – probability of radiative spontaneous transition, $B(JJ')$ – luminescence branching ratio, A_{tot} – total probability of radiative spontaneous transitions, τ_{rad} – radiative lifetime of the excited state, ED and MD – electric-dipole and magnetic-dipole contributions, respectively.